New DNS Results of Shockwave/Turbulent Boundary Layer Interaction

M. Wu*and M.P. Martin†

Mechanical and Aerospace Engineering Department

Princeton University, Princeton, NJ 08540

In previous direct numerical simulations[1] (DNS) of shockwave and turbulent boundary layer interactions we found significant discrepancies between the DNS and experimental data at the same flow conditions. Subsequent DNS[2] and analysis showed that numerical dissipation was responsible for the lack of agreement and we made improvements to the numerical method by introducing limiters in the smoothness measurement of the shock-capturing scheme. In this paper, we continue the study of limiters, which results in significantly reduced numerical dissipation. The new DNS data for a compression ramp configuration show good agreement with experiments. In particular, the upstream boundary layer, the mean wall-pressure distribution, the size of the separation bubble, the velocity profile downstream of the interaction and the mass-flux turbulence amplification factor downstream of the interaction are predicted within the experimental uncertainty. The motion of the shock and separation point are studied. The DNS data predict an amplitude of 1.2δ for the motion of the separation point. In contrast to higher Reynolds number experiments,[3] the wall-pressure fluctuation has a relatively low peak, 11% of the mean wall pressure versus 20%.

Nomenclature

M	Freestream Mach number
a	Speed of sound
δ	Thickness of the incoming Boundary layer
δ^*	Displacement thickness of the incoming Boundary layer
θ	Momentum thickness of the incoming Boundary layer
Re_θ	Reynolds number based on θ
Re_δ	Reynolds number based on δ
C_f	Skin friction coefficient
x	Coordinate in the streamwise direction
y	Coordinate in the spanwise direction
z	Coordinate in the wall-normal direction
Subscript	
∞	Freestream value
w	value at the wall

I. Introduction

Many aspects of shockwave and turbulent boundary layer interaction (STBLI) are not fully understood, including the dynamics of shock unsteadiness; turbulence amplification and mean flow modification induced by shock distortion; separation and reattachment criteria as well as the unsteady heat transfer near the

*Graduate Student, Student Member AIAA.

†Assistant Professor, Member AIAA.

	M	Re_θ	θ (mm)	δ^* (mm)	C_f	δ (mm)
Experiment[10]	2.9	2400	0.43	2.36	0.00225	6.7
DNS	2.9	2300	0.38	1.80	0.00210	6.4

Table 1. Conditions for the incoming turbulent boundary layer.

separation and reattachment points; and the generation of turbulent mixing layers and under-expanded jets in the interaction region, especially when they impinge on a surface. Yet, STBLI problems are of great importance for the efficient design of scramjet engines and control surfaces in proposed for hypersonic vehicles. A more profound understanding of STBLI will lead to flow control methodologies and novel hypersonic vehicle designs.

Much experimental and theoretical work has been done on STBLI. For example, Settles et al.[4,5] studied 2D/3D compression ramp and sharp fin STBLI problems, Dolling et al.[3,6] studied the unsteadiness for compression ramp configurations, and Selig[7] studied of the unsteadiness of STBLI and its control for a 24° compression ramp.

With the rapid development of computer power and capacity, it is now possible to perform detailed simulations of compressible turbulent flows. DNS provides time and space-accurate, three-dimensional flow data, that can be analyzed to gain physical understanding. However, the state-of-the-art numerical methods are not sufficiently robust to simulate general STBLI configurations, where the simulations require robust shock-capturing, high band-width resolution, and low dissipation. Weighted-essentially-non-oscillatory (WENO) methods are very promising. However, we have found them too dissipative for STBLI problems on affordable grids.[2] Modifications, however, can be made to reduce the inherent numerical dissipation in WENO methods.[8,9]

In this paper, we present new DNS data of STBLI using a modified WENO method. The flow configuration and numerical methods are presented in Section II. Details about the modified WENO method are presented in Section III. In Section IV, DNS data are compared with the experiments of Bookey et al.[10] at the same flow conditions. A discussion regarding the shock motion is presented in Section V, and we conclude our analysis in Section VI.

II. Flow configuration and numerical method

The configuration for the DNS is a compression ramp as shown in Figure 1. The angle of the ramp is 24°. We compare the DNS results with the reference experiment performed by Bookey et al.[10] for the same configuration. The flow conditions are shown in Table 1.

The governing equations are the non-dimensionalized conservative form of the continuity, momentum and energy equations in curvilinear coordinates. The working fluid is air, which is assumed to be a perfect gas.

$$\frac{\partial \boldsymbol{U}}{\partial t} + \frac{\partial \boldsymbol{F}}{\partial \xi} + \frac{\partial \boldsymbol{G}}{\partial \eta} + \frac{\partial \boldsymbol{H}}{\partial \zeta} = 0 \tag{1}$$

where

$$\boldsymbol{U} = J \begin{Bmatrix} \rho \\ \rho u \\ \rho v \\ \rho w \\ \rho e \end{Bmatrix}, \quad \boldsymbol{F} = \boldsymbol{F}_c + \boldsymbol{F}_v \tag{2}$$

and

$$\boldsymbol{F}_c = Jr_\xi \begin{Bmatrix} \rho u' \\ \rho u u' + p s_x \\ \rho v u' + p s_y \\ \rho w u' + p s_z \\ (\rho e + p) u' \end{Bmatrix}, \quad \boldsymbol{F}_v = -Jr_\xi \begin{Bmatrix} 0 \\ \sigma_{xx} s_x + \sigma_{xy} s_y + \sigma_{xz} s_z \\ \sigma_{yx} s_x + \sigma_{yy} s_y + \sigma_{yz} s_z \\ \sigma_{zx} s_x + \sigma_{zy} s_y + \sigma_{zz} s_z \\ (\sigma_{xx} u + \sigma_{xy} v + \sigma_{xz} w) s_x + \\ (\sigma_{yx} u + \sigma_{yy} v + \sigma_{yz} w) s_y + \\ (\sigma_{zx} u + \sigma_{zy} v + \sigma_{zz} w) s_z - \\ q_x s_x - q_y s_y - q_z s_z \end{Bmatrix} \tag{3}$$

$$s_x = \xi_x / r_\xi, \; u' = u s_x + v s_y + w_s z, \; r_\xi = \sqrt{\xi_x^2 + \xi_y^2 + \xi_z^2} \tag{4}$$

σ_{ij} is given by Newtonian linear stress-strain relation:

$$\sigma_{ij} = \frac{1}{Re_\delta} \left(2\mu S_{ij} - \frac{2}{3} \mu \delta_{ij} S_{kk} \right) \tag{5}$$

The heat flux terms q_j are given by Fourier law:

$$q_j = -\frac{1}{Re_\delta} k \frac{\partial T}{\partial x_j} \tag{6}$$

The non-dimensionalization is done by $\rho = \rho^*/\rho^*_\infty$, $u = u^*/U^*_\infty$, $e = e^*/U^{*2}_\infty$, and $T = T^*/T^*_\infty$. Here $*$ denotes dimensional quantities and ∞ denotes freestream quantities. Incoming boundary layer thickness δ is used as the characteristic length scale.

We use a 4th-order bandwidth-optimized WENO[11] (weighted-essentially-non-oscillatory) method to compute the convective flux terms. It is found that original the WENO methods are too dissipative for the DNS of STBLI problems on affordable grids.[2] In this paper, we use a modified WENO method and details are presented in the next section. A 3rd-order accurate low-storage Runge-Kutta method is used for the time integration, and a 4th-order accurate central standard finite difference scheme is used to compute the viscous flux terms.

To minimize numerical errors in the computation of Jacobian matrices, we generate the grid using analytical transformations. Details about the transformation can be found in the reference.[12] A sample grid is plotted in Figure 2. The grid is clustered near the corner in the streamwise direction and near the wall in the wall-normal direction. The size of the computational domain is shown in Figure 3. We have 9δ and 7δ upstream and downstream of the corner in the streamwise direction, 2.2δ in the spanwise direction, and 5δ in the wall-normal direction. The number of grid points used in the DNS is $1024 \times 160 \times 128$ in the streamwise, spanwise, and wall-normal directions, respectively. The largest and smallest grid spacings in the streamwise direction are $\Delta x^+ = 7.2$ and $\Delta x^+ = 3.4$, respectively. The grid spacing in the spanwise direction is $\Delta y^+ = 4.1$. In the wall-normal direction at the inlet, the first grid is at $z^+ = 0.2$.

The rescaling method developed by Xu & Martin[13] is used to generate the inflow condition. Supersonic outflow boundary conditions are used at the outlet and the top boundary. We use non-slip condition at the wall, which is isothermal. Details about initial and boundary conditions can be found in the references.[1,12]

III. Modification of original WENO method

We use a WENO method to compute convective flux terms. In WENO, numerical fluxes are approximated by the weighted sum of fluxes on the candidate stencils. Figure 4 plots a sketch of the WENO three-point candidate stencils. The numerical flux can be expressed as:

$$f_{i+\frac{1}{2}} = \sum_{k=0}^{r} \omega_k q_k^r \; , \tag{7}$$

where q_k^r are the candidate fluxes at $(i + 1/2)$ and ω_k are the weights. The weights are determined by the smoothness on each candidate stencil, where the smoothness is measured by:

$$IS_k = \sum_{m=1}^{r-1} \int_{x_{i-1/2}}^{x_{i+1/2}} (\Delta x)^{2m-1} \left(\frac{\partial^m q_k^r}{\partial x^m} \right)^2 dx \tag{8}$$

Thus, larger weights are assigned to stencils with smaller IS_k. For the three-point per candidate stencil WENO shown in Figure 4, Taylor expansion of the above equation gives:

$$IS_k = \left(f_i' \Delta x\right)^2 \left(1 + O(\Delta x^2)\right) \tag{9}$$

This means that in smooth regions for a well resolved flow field (meaning f_i' is O(1)), IS_k is of the order of Δx^2. While for a discontinuity, IS_k is of the order of 1. Details about the formulation of WENO methods can be found in Jiang & Shu[14] and Martin et al.,[11] for example.

The above argument is made with the assumption that all the scales in the simulation are well resolved. In turbulent flows, there is a wide range of scales. With the power and capacity of current computers, it is infeasible to have a descent resolution for the smallest scales, which are the Kolmogrov's scales. Here descent resolution means that for a smooth function f, there are enough grid points to resolve it so that the numerical approximation of the derivative f' computed on these grid points is of $O(1)$. For small scales in our DNS, the above arguments about the smoothness measurement of WENO do not hold (f_j' can be very large for smooth data). The result is that too much dissipation is added at small scales. To mitigate the problem, we proposed adding limiters in the smoothness measurement.[8] There are two kinds of limiters: absolute limiter and relative limiter. The definitions of the absolute and relative limiters are shown below in Equation 10 and 11, respectively.

$$\omega_k = \begin{cases} C_k^r, \ if \ max(IS_k) < A_{\mathrm{AL}} \\ \omega_k, \ otherwise \end{cases} \tag{10}$$

$$\omega_k = \begin{cases} C_k^r, \ if \ max(IS_k)/min(IS_k) < A_{\mathrm{RL}} \\ \omega_k, \ otherwise \end{cases} \tag{11}$$

It is found that the relative limiter is more general and less problem depend.[8] However, it turns out that the relative limiter defined by Equation 11 is method dependent, i.e. WENO methods with different candidate stencil sizes have different threshold values in the relative limiter. Here we use a modified relative limiter:

$$\omega_k = \begin{cases} C_k^r, \ if \ max(TV_k)/min(TV_k) < A_{\mathrm{RL}}^{\mathrm{TV}} \\ \omega_k, \ otherwise \end{cases}, \tag{12}$$

where TV_k stands for the total variation on each candidate stencil. The new definition allows more consistent threshold values of about 5 in the relative limiter. The performance of the new limiter for the 4th-order bandwidth-optimized WENO scheme is tested by computing the Shu-Osher problem.[15] The initial conditions are:

$$\begin{cases} \rho_l = 3.86, \ \rho_r = 1 + 0.2sin(5x) \\ u_l = 2.63, \ u_r = 0 \\ p_l = 10.33, \ p_r = 1 \end{cases} \tag{13}$$

Figure 5 plots the results at $t = 1.8$. The line is the converged numerical result using 1600 grid points. The square and triangle symbols are the computed results with and without the relative limiter using 200 grid points, respectively. It is clear that the result with the relative limiter is much better in the high frequency fluctuation region, where the resolution is poor.

We also found that the absolute limiter alone improved our DNS results for the compression ramp case.[2] In what follows, we show that using both the limiters at the same time reduces the numerical dissipation further, thereby improving the DNS results further. According to the definition of both the limiters, we see they have different effects on reducing the numerical dissipation. To show the effects of applying the limiters more clearly, 2D nonlinearity index contour plots computed in the wall-normal direction for the DNS of the compression ramp case are shown in Figure 6. The nonlinearity index is defined as:[16]

$$NI = \frac{1}{(r(r+1))^{1/2}} \left[\sum_{k=0}^{r} \left(\frac{\frac{1}{r+1} - \frac{\alpha_k / C_k^r}{\sum_{k=0}^{r} (\alpha_k / C_k^r)}}{\frac{1}{r+1}} \right)^2 \right]^{1/2} \tag{14}$$

It has a value in the range of [0,1]. The magnitude of NI indicates how much dissipation is added by WENO. The smaller NI is, the less dissipation is added. Ideally, NI should be zero everywhere except for regions

near discontinuities. Figure 6(a) shows that without any limiter, the nonlinearity index has high values in a very large region of the computational domain. Because in WENO methods, numerical fluxes are computed in the characteristic space, the NI values plotted here are also computed in the characteristic space for the characteristics equation with eigen-value equal to $u + a$. The average NI value is about 0.5. With the absolute limiter added, the dissipation is reduced greatly, as shown in Figure 6(b). The average NI value is 0.09. The same plot with the relative limiter is shown in Figure 6(c). The average NI value is also about 0.09 for this case. With both the relative and absolute limiters, as shown in Figure 6(d), the average NI value is 0.02, indicating the numerical dissipation is further reduced. In the DNS, we apply both limiters. However, the simulation can be unstable, and we find that this can be avoided by changing the relative limiter to:

$$\omega_k = \begin{cases} C_k^r, \; if \; max(TV_k)/min(TV_k) < A_{\mathrm{RL}}^{\mathrm{TV}} \; and \; max(TV_k) < B_{\mathrm{RL}}^{\mathrm{TV}} \\ \omega_k, \; otherwise \end{cases} \tag{15}$$

The additional threshold value $B_{\mathrm{RL}}^{\mathrm{TV}}$ guarantees enough dissipation whenever $max(TV_k)$ is larger than the threshold. The threshold values are $A_{\mathrm{AL}} = 0.01$, $A_{\mathrm{RL}}^{\mathrm{TV}} = 5$, and $B_{\mathrm{RL}}^{\mathrm{TV}} = 0.2$ in the DNS.

IV. DNS statistics

Statistics are gathered using 100 flow fields with time intervals equal to $0.5\delta/U_\infty$. Figure 7 is an instantaneous iso-surface contour plot of the magnitude of pressure gradient $|\nabla p| = 0.5$ for the DNS. It shows the 3D shock structure. Except for the foot of the shock, which is inside the boundary layer edge, the shock is quite flat in the spanwise direction. Also a few shocklets that merge into the main shock are visible. They are formed due to the compression at the reattachment point.

Figure 8 plots an instantaneous numerical schlieren plot, in which the variable is defined as:

$$NS = c_1 EXP(-c_2(x - x_{min})/(x_{max} - x_{min})) \tag{16}$$

where $x = |\nabla\rho|$ and c_1 and c_2 are constants. We use $c_1 = 0.8$ and $c_2 = 10$ in our analysis. The main shock wrinkles and the shock foot penetrates into the boundary layer. A few shocklets emanate from the edge of the boundary layer downstream of the interaction and they merge into the main shock eventually. The turbulence structures in the incoming boundary layer and downstream of the interaction are clearly seen. Downstream of the interaction, the gradients are steeper, showing the turbulence amplification due to the flow through the shock. Figure 9 plots the time and spanwise averaged numerical schlieren. The turning of the flow at the separation bubble upstream of the corner, results in the first portion of the main shock, which is at 29° and corresponds to an 11° turning angle. Near the reattachment point, the flow is turned again by the ramp wall. Compression waves can be seen in Figure 9. These waves are actually the averaged shocklets shown in Figure 8. They merge into the main shock at a location of about 4δ downstream of the corner and change the angle of the main shock. The second part of the shock has an angle of about 37°, which is still less than that of an inviscid shock angle (43°). This is because the computational domain is not long enough to let the shock evolve further.

The DNS are compared with the experiments of Bookey et al.[10] Figure 10 plots the mean wall-pressure distribution. Error bars of 5% are plotted for the experimental data. The DNS data predict the pressure distribution within the experimental uncertainty, including the pressure plateau. Figure 11 plots the non-dimensionalized size of the separation bubble versus Reynolds number. The characteristic length is defined as:

$$L_c = \frac{\delta}{M^3}\left(\frac{p_2}{p_{pl}}\right)^{3.1}, \tag{17}$$

where p_2 is the downstream inviscid pressure and p_{pl} is the plateau pressure. The data points for the DNS and the reference experiment both lie within the empirical envelop. The difference between them is about 10%. The predicted separation and reattachment points are at $x = -3\delta$ and $x = 1.3\delta$, respectively (the corner is located at $x = 0$). While in the experiment of Bookey et al., the separation and reattachment points are at $x = -3.2\delta$ and $x = 1.6\delta$, respectively.

Figure 12 plots the comparison of the velocity profile 4δ downstream of the corner. The velocity is non-dimensionalized by that at the boundary layer edge. The agreement is good except for the near wall region, where experimental data have large errors. Figure 13 plots mass flux turbulence intensities at different streamwise locations for the DNS. Downstream of the interaction, we see that the maximum of the

mass flux turbulence intensity is amplified by a factor of 5, which is consistent with the number 4.8 that Selig found in experiments.[17] Notice here the experiments of Selig are at a much higher Reynolds number ($Re_\theta = 85,000$). It is believed, however, that the mass flux turbulence intensity amplification is not Reynolds number dependent.

Figure 14 plots Van-Driest transformed mean velocity profiles at different streamwise locations. Near the inlet of the computational domain ($x = -8\delta$), the profile agrees well with the log law in the logarithmic region. The profile does not change at $x = -4.1\delta$, which is about 1δ upstream of the separation location. Downstream of the interaction, the profiles show characteristic dips in the logarithmic region, which is consistent with what Smits and Muck[18] found in higher Reynolds number ($Re_\theta = 85,000$) experiments. Figure 15 plots three velocity profiles at different streamwise locations. For the profile at $x = -1.9\delta$, which is inside the separation region, the velocity profile is very different from that at the inlet. It has a linear behavior. Downstream of the interaction, at $x = 6.1\delta$, the boundary layer profile is not recovered. Also notice that there is no visible oscillation near the shock, which means that the limiters presented in Section III do not affect the good shock-capturing properties of WENO.

Figure 16 plots the wall pressure fluctuation for the DNS. The normalized wall-pressure fluctuation has a peak value upstream of the corner near the separation point with a magnitude of 11%. There is a second peak downstream of the corner with a magnitude of 11% also. Currently, there are no experimental data at the same Reynolds number. According to higher Reynolds number experiments, the magnitude of the first peak is about 20%,[3] which is significantly higher than that of our DNS. This issue is further discussed in the next section.

V. Analysis of shock motion

Dolling and Or[6] found that the amplitude of the shock oscillation increases with ramp angle. For a 24° ramp with $M = 3$ and $Re_\theta = 85,000$, they report an amplitude of shock motion of about 0.8δ.

The shock foot is formed at the turning of the flow due to the separation bubble. To study the shock motion, we consider the motion of the separation point. In the recent experiments of Ganapathisubramani et al.,[19] they compute the location of the separation point using a threshold based technique, where the streamwise velocity u is measured in a streamwise-spanwise plane at a certain distance from the wall in the logarithmic region. Mean and standard deviation of u are measured for the incoming boundary layer at the same wall-normal location. Then, the first point in the streamwise location whose velocity is $u < (\langle u \rangle - 4u'_{\mathrm{RMS}})$ is set to be the separation point. Considering the same technique for the DNS data, we measure the location of the separation point at a wall-normal position in the logarithmic region, $z/\delta = 0.2$. The probability density function (PDF) of the separation location is plotted in Figure 17. The experimental result from Ganapathisubramani et al. is also plotted for reference. Despite the differences in the Mach number, Reynolds number, and ramp angle ($M = 2$, $Re_\theta = 35,000$, and ramp angle of 20° in the experiment of Ganapathisubramani et al.), the two PDFs have similar shape. For the DNS data, the PDF shows that the separation point moves in a range of about 2δ.

From the DNS, the instantaneous location of the separation point can be obtained more accurately by computing the skin friction coefficient at the wall. The history of the location of the separation point along the centerline of the computational domain is plotted in Figure 18. There are a number of bad points in the plot because the instantaneous skin friction coefficient at a point in the incoming boundary layer can also be less than zero due to large velocity fluctuations. Neglecting those points, the range of the motion of the separation point is about 1.2δ.

It is known that the high magnitude of the first peak of the wall-pressure fluctuation is caused by the large scale motion of the shock. As the shock moves upstream and downstream about some point, the instantaneous pressure measured at that point varies depending on the shock position. Thus, the shock motion generates wall-pressure fluctuations. Figure 19 plots the histories of the wall pressure at different streamwise locations along the centerline of the computational domain. Figure 20 plots three wall-pressure signals measured in Selig's experiment.[7] In the experiment, the boundary layer thickness is 26mm and the freestream velocity is about 580 m/s. The three signals were measured at $x = -1.8\delta$, $x = -1.95\delta$, and $x = -2.1\delta$, respectively. The separation point is at about $x = -1.7\delta$. The length of the signals is about $178\delta/U_\infty$. It is clear that the wall pressure signals for the DNS do not have the intermittent character that is observed in the experiments. This is consistent with the fact that the amplitude of the shock motion is lower in the DNS flow.

VI. Conclusion

DNS of a 24° compression ramp configuration is performed. Applying limiters to the smoothness measurement in the WENO scheme reduces the numerical dissipation. In particular, using a combination of absolute and relative limiters is very effective. Numerical schlieren and 3D iso-surfaces of $|\nabla p|$ plots reveal the structures of the shock system. The DNS data predicts the experiments within the experimental uncertainty for the upstream boundary layer, mean wall-pressure distribution, size of the separation bubble, velocity profile downstream of the interaction, and mass flux turbulence intensity amplification.

PDF and histories of the separation location are studied. The separation location moves in a range of about 1.2δ in the DNS. The experiments of Dolling and Or[6] predict an amplitude of shock motion of about 0.8δ. Histories of the wall-pressure signal are studied. At the separation point, the magnitude of the wall-pressure fluctuation is about 11% of the mean. The magnitude is lower than the 20% that is predicted in higher Reynolds number experiments.[3] Experiments to measure the wall-pressure fluctuations for the same flow conditions are on the way.

Acknowledgments

This work is supported by the Air Force Office of Scientific Research under grant AF/F49620-02-1-0361.

References

[1]Wu, M., Taylor, E. M., and Martin, M. P., "Assessment of STBLI DNS Data and Comparison against Experiments," *AIAA Paper No. 2005-4895, 35th AIAA Fluid Dynamics Meeting, Toronto, Canada*, 2005.

[2]Wu, M. and Martin, M. P., "Assessment of Numerical Methods for DNS of Shockwave/Turbulent Boundary Layer Interaction," *AIAA Paper No. 2006-0717, 44th AIAA Aerospace Science Meeting and Exhibit, Reno, NV*, 2006.

[3]Dolling, D. S. and Murphy, M. T., "Unsteadiness of the Separation Shock Wave in a Supersonic Compression Ramp Flowfield," *AIAA Journal*, Vol. 21, No. 12, 1983.

[4]Settles, G. S., Vas, I. E., and Bogdonoff, S. M., "Details of Shock-Separated Turbulent Boundary Layer at a Compression Corner," *AIAA Journal*, Vol. 14, No. 12, 1976, pp. 1709–1715.

[5]Settles, G. S., Fitzpartrick, T., and Bogdonoff, S. M., "Detailed Study of Attached and Separated Compression Corner Flowfields in High Reynolds Number Supersonic Flow," *AIAA Journal*, Vol. 17, No. 6, 1979.

[6]Dolling, D. S. and Or, C. T., "Unsteadiness of the Shock Wave Structure in Attached and Separated Compression Corner Flow Fields," *AIAA Paper No. 83-1715*, 1983.

[7]Selig, M. S., *Unsteadiness of Shock Wave/Turbulent Boundary Layer Interactions with Dynamic Control*, Ph.D. thesis, Princeton University, 1988.

[8]Taylor, E. M., Wu, M., and Martin, M. P., "Optimization of Nonlinear Error Sources for Weighted Essentially Non-oscillatory Methods in Direct Numerical Simulations of Compressible Turbulence," *AIAA Paper No. 2006-1091, 44th AIAA Aerospace Science Meeting and Exhibit, Reno, NV*, 2006.

[9]Taylor, E. M. and Martin, M. P., "On Synchronization of Weighted Essentially Non-Oscillatory Methods," *AIAA Paper No. 2006-3740, 36th AIAA Fluid Dynamics Conference and Exhibit*, 2006.

[10]Bookey, P. B., Wu, M., Smits, A. J., and Martin, M. P., "New Experimental Data of STBLI at DNS/LES Accessible Reynolds Numbers," *AIAA Paper No. 2005-309*, 2005.

[11]Martin, M. P., Taylor, E. M., Wu, M., and Weirs, V., "A Bandwidth-Optimized WENO Scheme for the Direct Numerical Simulation of Compressible Turbulence," *to appear in Journal of Computational Physics*, 2006.

[12]Wu, M. and Martin, M. P., "Direct Numerical Simulation of Shockwave/Turbulent Boundary Layer Interactions," *AIAA Paper No. 2004-2145*, 2004.

[13]Xu, S. and Martin, M. P., "Assessment of Inflow Boundary Conditions for Compressible Boundary Layers," *Physics of Fluids*, Vol. 6, No. 7, 2004.

[14]Jiang, G. and Shu, C., "Efficient Implementation of Weighted ENO Schemes," *Journal of Computational Physics*, Vol. 126, 1996.

[15]Shu, C.-W. and Osher, S., "Efficient implementation of essentially non-oscillatory shock-capturing schemes, II," *Journal of Computational Physics*, Vol. 83, 1989, pp. 32–78.

[16]Taylor, E. and Martin, M., "Stencil Adaption Properties of a WENO Scheme in Direct Numerical Simulations of Compressible Turbulence," *to appear in Journal of Scientific Computing*, 2006.

[17]Selig, M. S., Muck, K. C., Dussauge, J. P., and Smits, A. J., "Turbulent Structure in a Shock Wave/Turbulent Boundary-Layer Interaction," *AIAA Journal*, Vol. 27, 1989, pp. 862–869.

[18]Smits, A. and Muck, K., "Experimental study of three shock wave/turbulent boundary layer interactions," *Journal of Fluid Mech.*, Vol. 182, 1987, pp. 291–314.

[19]Ganapathisubramani, B., Clemes, N. T., and Dolling, D. S., "Planar imaging measurements to study the effect of spanwise structure of upstream turbulent boundary layer on shock induced separation," *AIAA Paper No. 2006-324, 44th AIAA Aerospace Meeting and Exhibit, Reno, NV*, 2006.

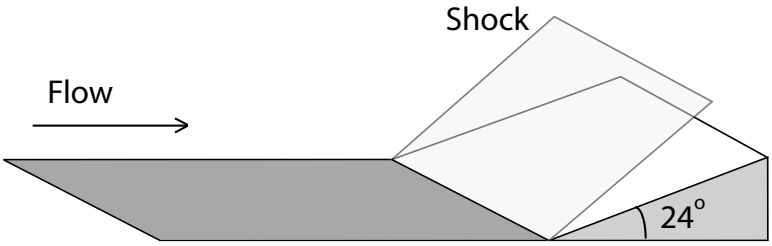

Figure 1. Inviscid flow cartoon for the compression ramp case.

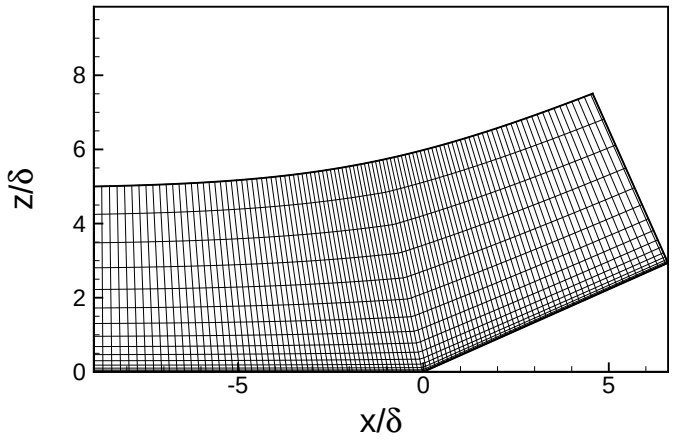

Figure 2. Sample grid for the compression ramp case.

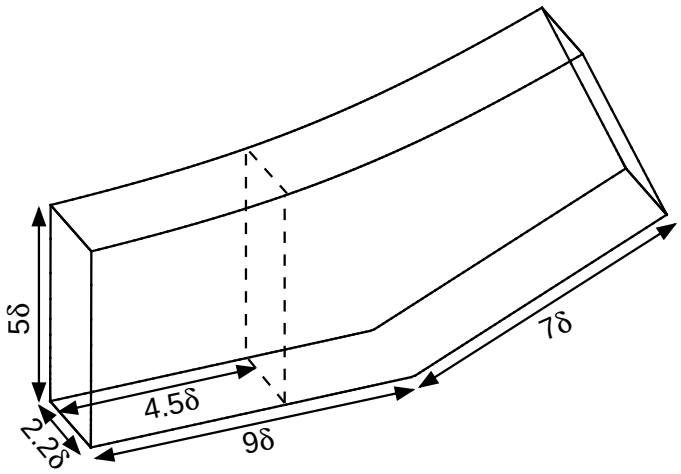

Figure 3. Size of the computational domain for the DNS.

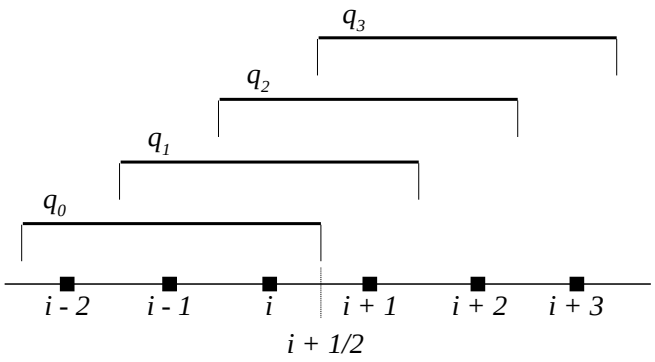

Figure 4. Sketch of WENO candidate stencils with 3 points per candidate stencil.

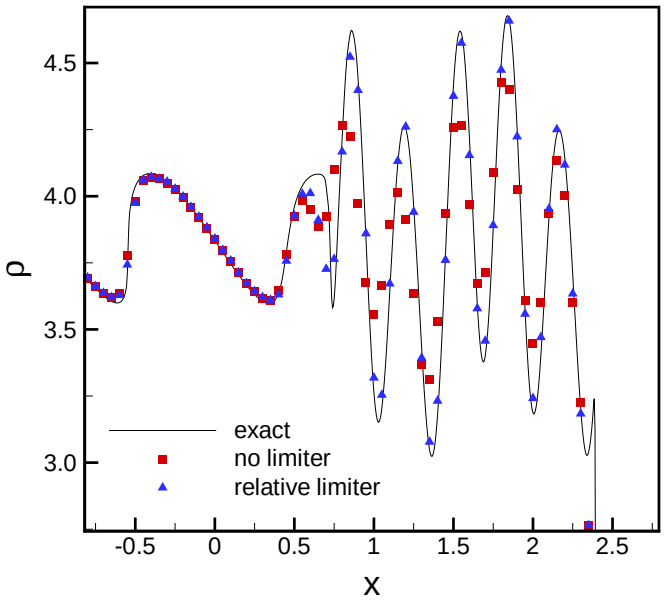

Figure 5. Density distribution at $t = 1.8$ for the Shu-Osher's problem with and without the relative smoothness limiter.

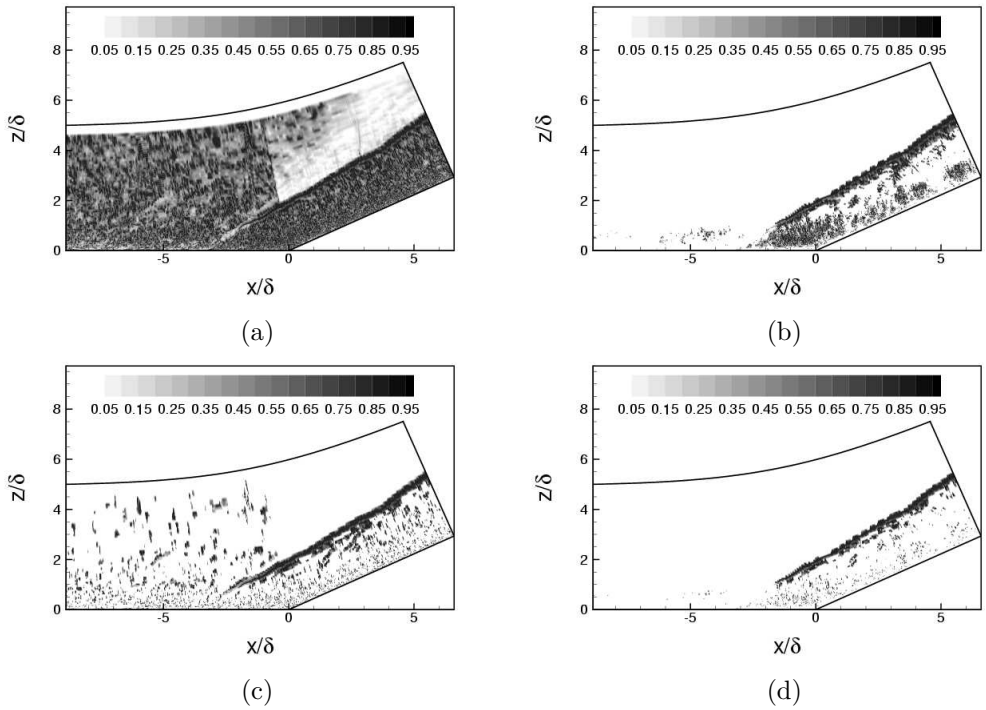

Figure 6. Nonlinearity index for the compression ramp case: (a) without limiters, (b) with the absolute limiter, (c) with the relative limiter, and (d) with both the relative and absolute limiters.

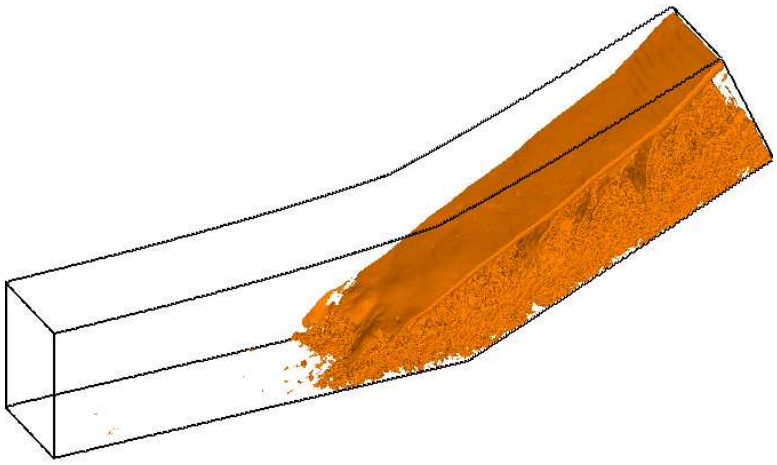

Figure 7. Contour plot of the magnitude of the pressure gradient, $|\Delta P| = 0.5$, showing the 3D shock structure from DNS data.

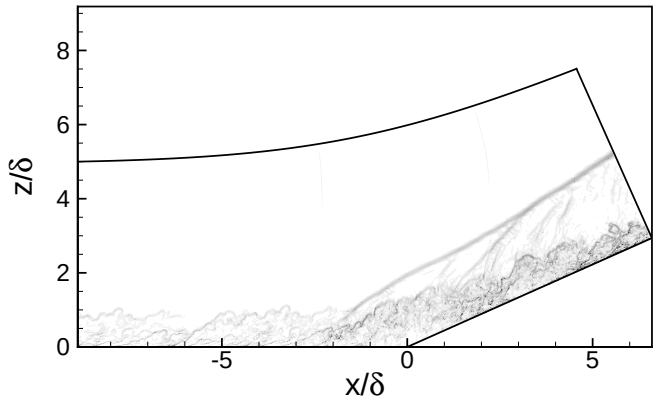

Figure 8. Instantaneous numerical schlieren plot from DNS data.

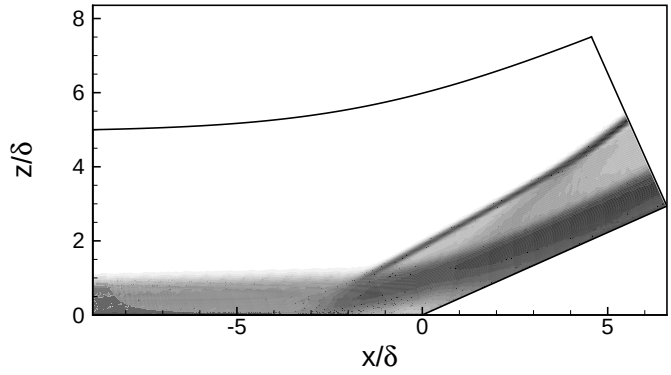

Figure 9. Time and spanwise averaged numerical schlieren plot from DNS data.

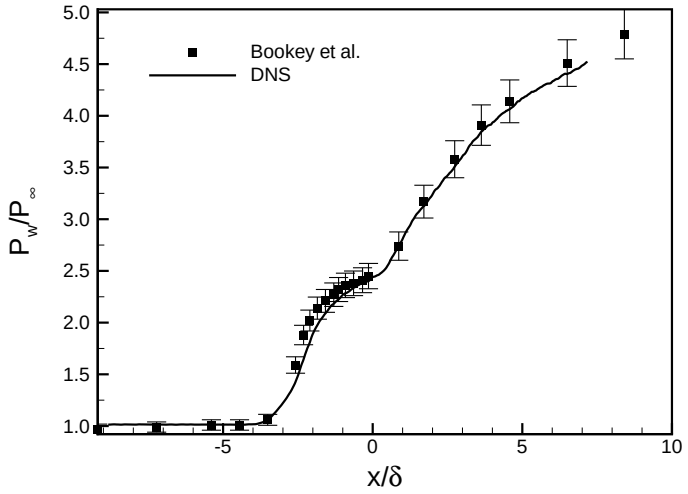

Figure 10. Mean wall-pressure distribution from DNS and experimental data. Error bars at 5%.

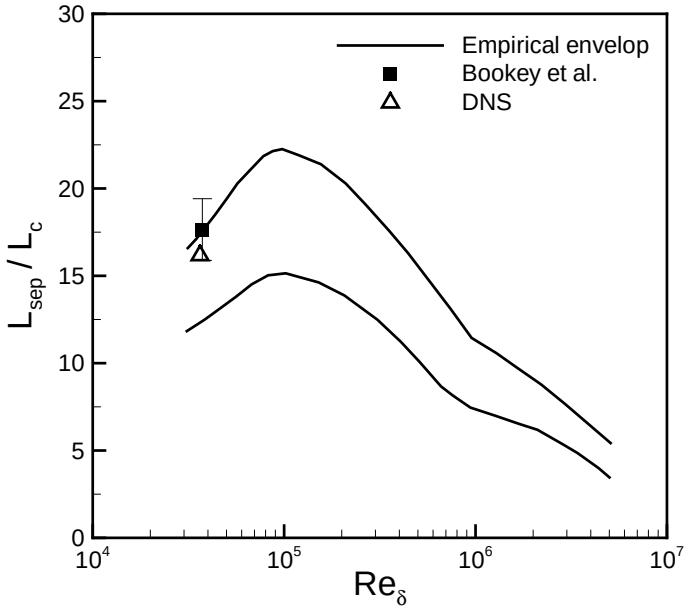

Figure 11. Size of the separation bubble from DNS and experimental data. Error bars at 10%.

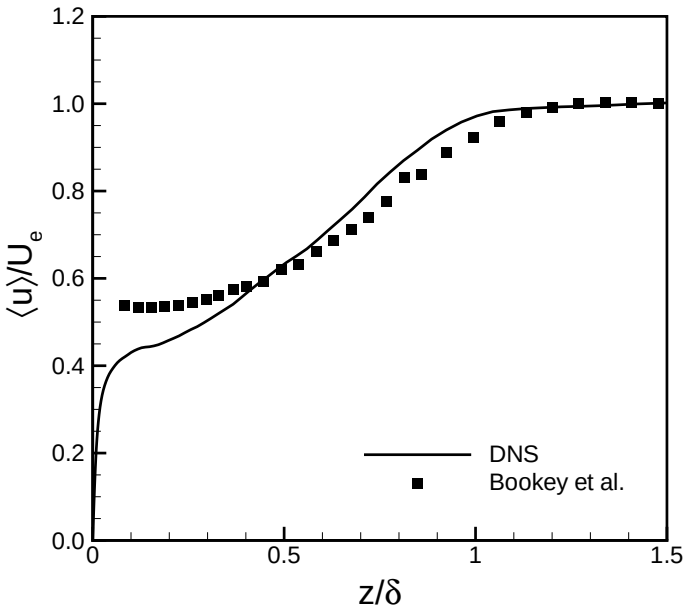

Figure 12. Velocity profile 4δ downstream of the corner from DNS and experimental data.

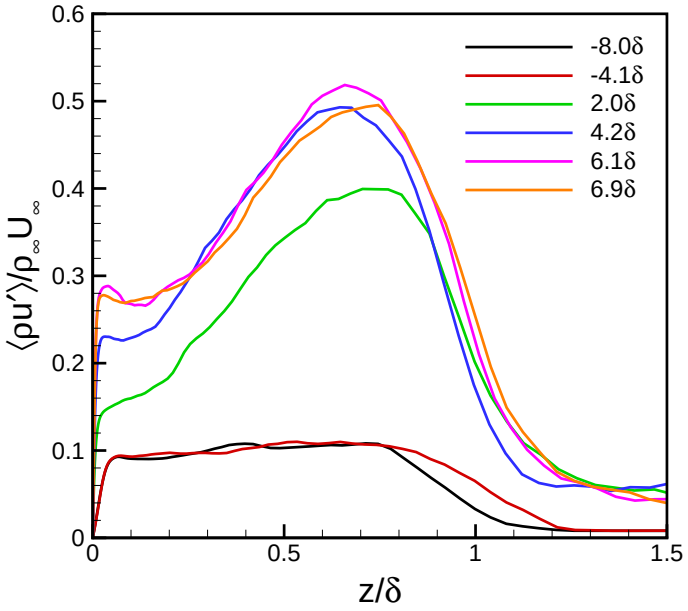

Figure 13. Mass flux turbulence intensities at different streamwise locations from DNS data.

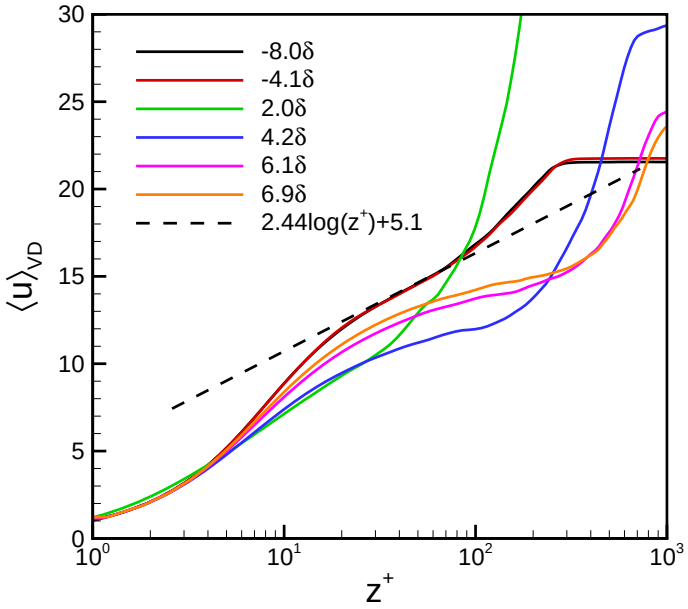

Figure 14. Van-Driest transformed mean velocity profiles at different streamwise locations from DNS data.

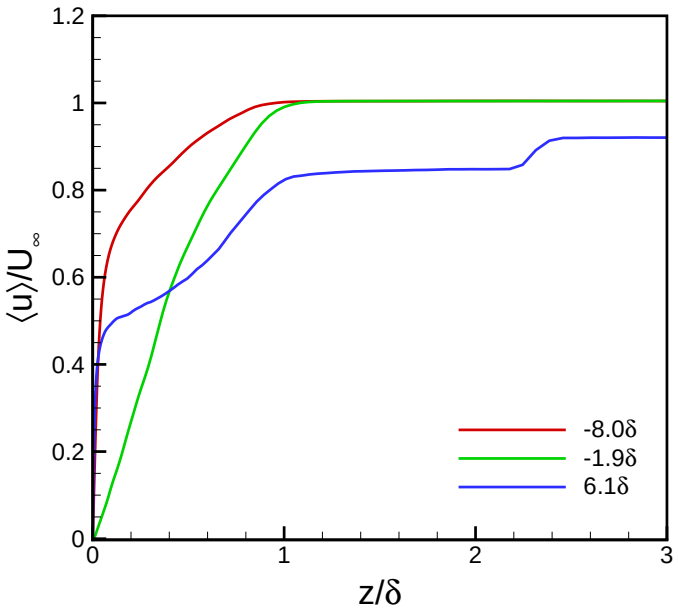

Figure 15. Velocity profiles at three different streamwise locations from DNS data.

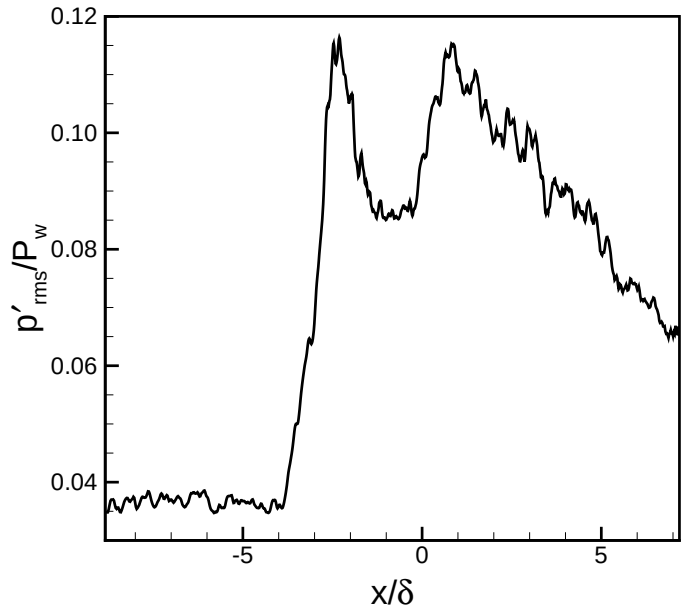

Figure 16. Wall-pressure fluctuation distribution from DNS data.

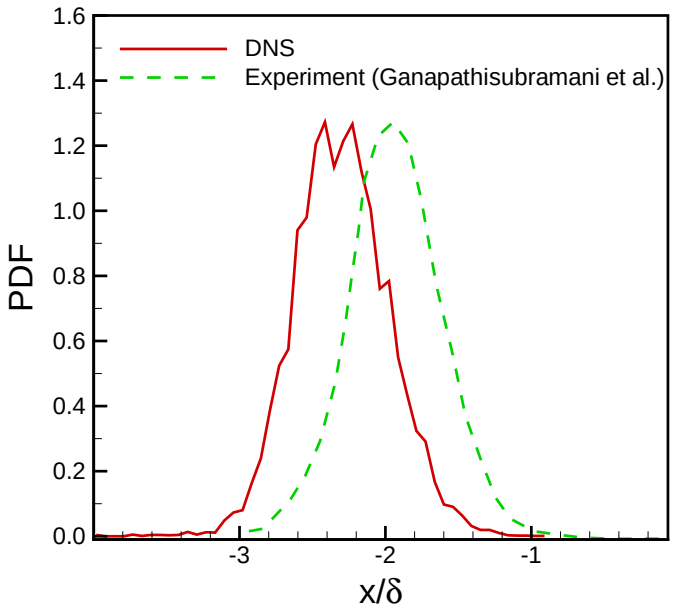

Figure 17. Probability density function of the separation location at $z/\delta = 0.2$ from DNS data.

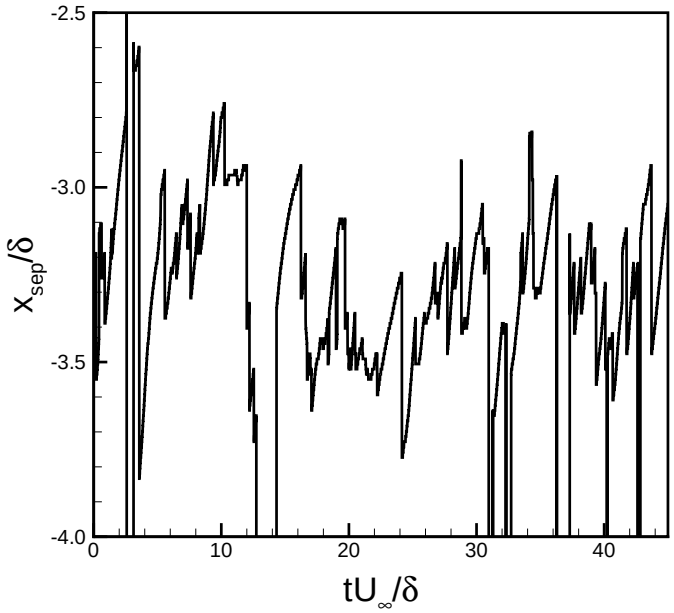

Figure 18. History of the location of the separation point along the center line from DNS data.

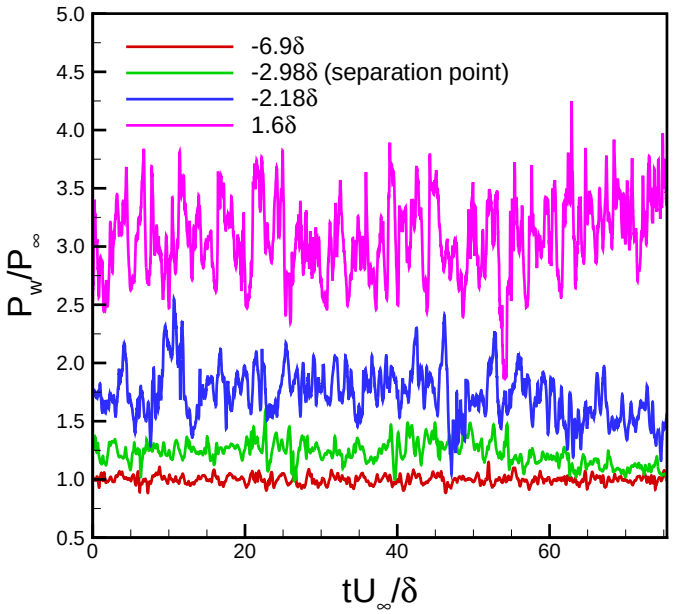

Figure 19. Histories of the wall pressure at different streamwise locations from DNS data.

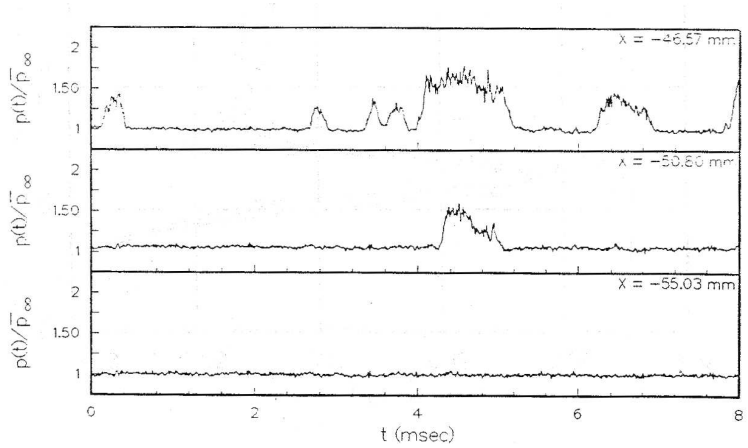

Figure 20. Histories of the wall pressure at different streamwise locations from Selig's experiment.

36th AIAA Fluid Dynamics Conference, June 5–8, 2006/San Francisco,California

New DNS Results of Shockwave/Turbulent Boundary Layer Interaction

M. Wu*and M.P. Martin†

Mechanical and Aerospace Engineering Department

Princeton University, Princeton, NJ 08540

Amendment

The empirical envelop in Figure 11 together with the characteristic length scale defined in Equation 17 are obtained from Zheltovodov et al.[1]

1. Zheltovodov, A. A., Schülein, E., and Horstman, C., "Development of separation in the region where a shock interacts with a turbulent boundary layer perturbed by rarefaction waves," Journal of Applied Mechanics and Technical Physics, Vol. 34, No. 3, 1993, pp. 346-354

*Graduate Student, Student Member AIAA.

†Assistant Professor, Member AIAA.